Terahertz electronic and optoelectronic components and systems

Imaging by terahertz photon counting

Comptage de photons pour l'imagerie térahertz

Kenji Ikushima [a,b,*], Susumu Komiyama [c]

[a] *Department of Applied Physics, Tokyo University of A & T, Naka-cho, Koganei, Tokyo 184-8588, Japan*
[b] *PRESTO, JST, 4-1-8 Honcho Kawaguchi, Saitama 332-0012, Japan*
[c] *Department of Basic Science, University of Tokyo, Komaba, Meguro-ku, Tokyo 153-8902, Japan*

A B S T R A C T

Photon counting method is indispensable in visible/near-infrared optical measurements for detecting extremely weak radiation. The method, however, has been inaccessible in terahertz region, where the photon energies are more than 100 times smaller and catching individual photons is difficult. Here we review photon counting measurements of terahertz waves, by incorporating a semiconductor quantum-dot terahertz-photon detector into a scanning terahertz microscope. By using a quantum Hall effect detector as well, measurements cover the intensity dynamic range more than six orders of magnitude. Applying the measurement system to the study of semiconductor quantum Hall effect devices, we image extremely weak cyclotron radiation emitted by nonequilibrium electrons. Owing to the unprecedented sensitivity, a variety of new features of electron kinetics are unveiled. Besides semiconductor electric devices studied here, the experimental method will find application in diverse areas of molecular dynamics, microthermography, and cell activities.

© 2010 Académie des sciences. Published by Elsevier Masson SAS. All rights reserved.

R É S U M É

Les techniques de comptage de photons se révèlent indispensables pour détecter des rayonnements visibles ou infrarouges très peu intenses. Dans le domaine des ondes térahertz, ces techniques n'étaient pas employées jusqu'à présent, car elles sont rendues très difficiles à mettre en œuvre à cause de l'énergie très faible de chaque photon térahertz, qui est au moins 100 fois plus faible que celle des photons infrarouges ou visibles. Dans ce papier, nous donnons une revue des récentes techniques de comptage de photons térahertz, réalisées à l'aide de détecteurs de type boite quantique à semi-conducteur, qui nous ont permis de construire un microscope térahertz à balayage. La dynamique de détection est augmentée de 6 ordres de grandeur grâce à l'effet Hall quantique dans les détecteurs. Nous avons utilisé notre microscope térahertz pour étudier des composants semi-conducteurs à effet Hall quantique. Ainsi, nous avons pu imager le très faible rayonnement cyclotron émis par un gaz d'électrons hors équilibre. Grâce à la sensibilité inégalée de notre instrument, nous avons mis en évidence des phénomènes de dynamique des électrons pas encore observés. En plus des études des composants à semi-conducteurs reportées ici, notre dispositif pourra être employé dans différents domaines scientifiques comme la dynamique moléculaire, la micro-thermographie, ou l'activité cellulaire en biologie.

© 2010 Académie des sciences. Published by Elsevier Masson SAS. All rights reserved.

* Corresponding author.
 E-mail address: ikushima@cc.tuat.ac.jp (K. Ikushima).

1. Introduction

For spectroscopic studies, the terahertz region (1 THz $\sim$ 33 cm^{-1} or 4 meV) distinguishes itself by the richness of contained spectra of matter. Techniques for generating and controlling THz waves have been renovated in recent years, being exemplified by several new developments including the generation of THz waves exploiting ultra-short visible laser pulses [1], time-domain spectroscopy [2], and semiconductor quantum cascade lasers [3]. The renovation has stimulated discussion about possible applications of THz waves to sensing, imaging and spectroscopy in diverse areas like clinics, security, and environment [2,4–6]. Since room-temperature operation is implicit in these applications, the radiation treated is relatively intense, being well beyond black-body radiation at 300 K (roughly 10^{-7} watts or 10^{14} photons/s per square centimeter in a 10% relative band width).

Aside from such applications on the everyday-life level, there can be another important approach; that is, to detect and to study ultimately weak THz radiation. While astronomers have long pursued this approach, researchers in basic research area of matters may benefit greatly as well. Photon energies of THz radiation are smaller than the thermal energy at room temperature (25 meV at 300 K). It follows that most matter readily emits THz radiation in not specifically arranged conditions. If the object is in thermal equilibrium, the radiation spectrum would be similar to that of black-body radiation, hence, uninteresting. However, objects of interest are rarely in a thermal equilibrium state: Most important effects, whether physical, chemical or biological phenomena, are manifestations of nonequilibrium states. In many conditions, any microscopic object may pick available energy from its environment, transform the energy into its intrinsic mode of excitation, create THz photons in which the information is imprinted, and emit them. Catching those photons via a sensitive microscope may contribute greatly to the study of local phenomena occurring within the objects. In conventional scheme of microscopy, however, an object is irradiated by an external source: the external radiation enforces excitation of the object, hindering such "intrinsic" emission by the objects. For the study of intrinsic dynamics of matters, therefore, passive microscopy, in which radiation emitted by the object without external irradiation is studied, is highly desirable.

Thermography is one example of a passive method, but its application has been limited because of restricted spectral and spatial resolutions. In general, passive microscopy has so far been relatively unexplored despite its potential importance. This is because the radiation to be detected can be extremely weak and sufficiently sensitive microscopes were not readily available. Recently, however, the situation is beginning to change. While the development of superconducting sensors is expanding the spectral range of photon counting towards the infrared region [7,8], photon counting has been realized in the THz/GHz region with semiconductor quantum-dot (QD) detectors [9,10]. Highly sensitive microscopy in the THz region is hence possible if one successfully combines those QD detectors with appropriately designed microscopes. A spectral resolution of $\Delta\lambda/\lambda < 0.05$ is obtained by a narrow bandwidth of the detectors, where the wavelength of the maximum sensitivity is magnetically tunable over $\lambda = 120$–170 μm. The highest sensitivity achieved in this actual measurement is about 0.1 count per second at $\lambda \sim 130$ μm. This corresponds to the incidence of about one photon per second, or 10^{-21} watt, on the detector, and is roughly about 1000 times more sensitive than the level of present astronomy. In Section 2, the design concept of the QD detectors and their actual operation conditions will be reviewed. In Section 3, photon-counting THz imaging with QD detectors will be described.

2. Single photon detection of THz waves

2.1. Sensitivity limit of conventional detectors

Detection sensitivity is generally defined as an incident optical power which gives signal-to-noise ratio of unity, $S/N = 1$, at a given bandwidth Δf: we call it the noise equivalent power, *NEP*. Since the noise current (or voltage) is proportional to the photosensitive area of the detector $\sqrt{A}$, a reciprocal value of the *NEP* normalized by $\sqrt{A}$ is used as an index to detector performance, so-called, the specific detectivity, $D^* = \sqrt{A}\sqrt{\Delta f}/(NEP)$ [cm Hz$^{1/2}$/W]. The specific detectivity D^* of conventional infrared photodetectors is shown in Fig. 1. We note here that, aside from the electrical noise attributed to the detector itself, there exist random variations in current (or voltage) caused by statistical photon fluctuation of thermal radiation from environments. The detector performance is thus limited when operated at room temperatures. The performance limit D^*_{BLIP} (background limited infrared performance) is shown as the solid curve in Fig. 1, where we assume that black-body radiation at 300 K enters the detector from a viewing angle of 2π with quantum efficiency $\eta = 1$.

The passive THz microscopy we mentioned above is deemed to be an attempt to measure photon fluctuations of spontaneous radiation in space and time, so to speak, to measure photon noise precisely. Therefore, detector sensitivity required for the passive microscopy should be far beyond D^*_{BLIP}. Considering loss of the optical system and $\eta < 1$ in actual measurements, the sensitivity required for the passive microscopy, D^*_{passive}, would be roughly three orders of magnitude larger than the D^*_{BLIP}. As shown in Fig. 1, there are few conventional detectors that greatly exceed the D^*_{passive}.

2.2. Quantum-dot single photon detectors

The utility of the photon counting method for low light level microscopy has led to its widespread use in the visible/near-infrared spectral region. Owing to a new type of QD single photon detectors, the method is now available in the THz spectral
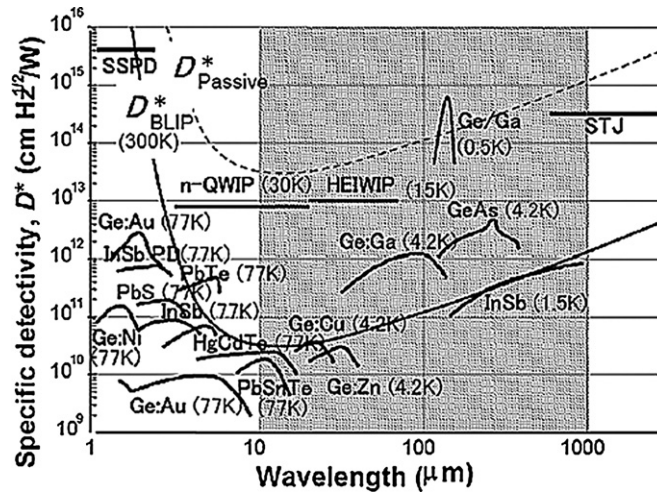
Fig. 1. Specific detectivity D^* of conventional infrared detectors. The operating temperature is shown in parentheses.

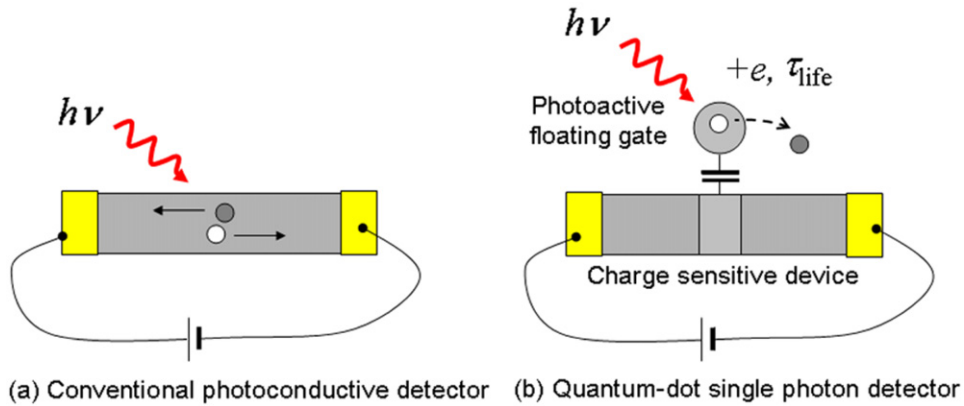(a) Conventional photoconductive detector (b) Quantum-dot single photon detector

Fig. 2. Schematics of conventional photoconductive detectors (a) and charge sensitive THz detector (b).

region. In the first half of this section, QD detectors and its family are briefly reviewed. In the last half, its actual operation condition is described.

Fig. 2 shows schematic illustrations of a conventional infrared photoconductive detector (a) and a QD single photon detector (b). In the conventional photoconductive detector, a single photon absorption event excites one nonequilibrium electron and the excess energy rapidly diffuses to the electron systems. Accordingly, the event is measured as a photocurrent signal I_{sig} of which the upper limit is described by $(P/h\nu)e$ (e is unit charge, P the incident light power and $h\nu$ the photon energy). This gives photoconductive detectors the upper limit of D^*. On the other hand, in the QD detector, the single photon absorption is converted to a long-lived unit charge in a floating gate without any diffusion process as schematically shown in Fig. 2(b). The floating gate, formed by semiconductor quantum structures, serves as a photon absorber from which one photoexcited electron escapes over a potential barrier. Missing one electron, the floating gate is charged up by $+e$, which is, in turn, sensitively detected by current change in a charge sensitive device, for instance, a single electron transistor (SET). The point is that the single photon absorption event is probed by a current change associated with G electrons, where $G \equiv (\Delta I \tau_{life})/e$ is much larger than unity (ΔI is a current change per unit charge in the charge sensitive device and τ_{life} is the photoexcited life time). In other words, the QD detector possesses in itself an integral function for the life time τ_{life}. The signal current I_{sig} is thereby amplified by a factor of G ($I_{sig} = G \times (P/h\nu)e$). Earlier works report $\tau_{life} = 10^{-8}$–10^3 s, yielding the amplification factor $G = 10^4$–10^{12} [11]. As the result, the extraordinarily large D^* is achieved and single photon detection becomes possible in the THz spectral region.

A family of QD detectors is categorized into two types by photon absorption mechanisms. One is a single QD with a strong magnetic field B where a THz photon is absorbed via cyclotron resonance (Type I) [9]. The center wavelength λ (center frequency f_c) is tuned to a range of 0.1–0.2 mm (1.5–3.0 THz) by the strength of B. Another type is a double QD system ($\lambda \sim 0.6$ mm or 0.5 THz) or a hybrid system between a metallic SET and a semiconductor QD ($\lambda > 0.2$ mm or $f_c < 1.5$ THz), by which a photon is absorbed via plasma resonance in the isolated QD (Type II) [10,12,13]. Furthermore, a new type of phototransistor with a semiconductor floating gate has been also developed based on double quantum well
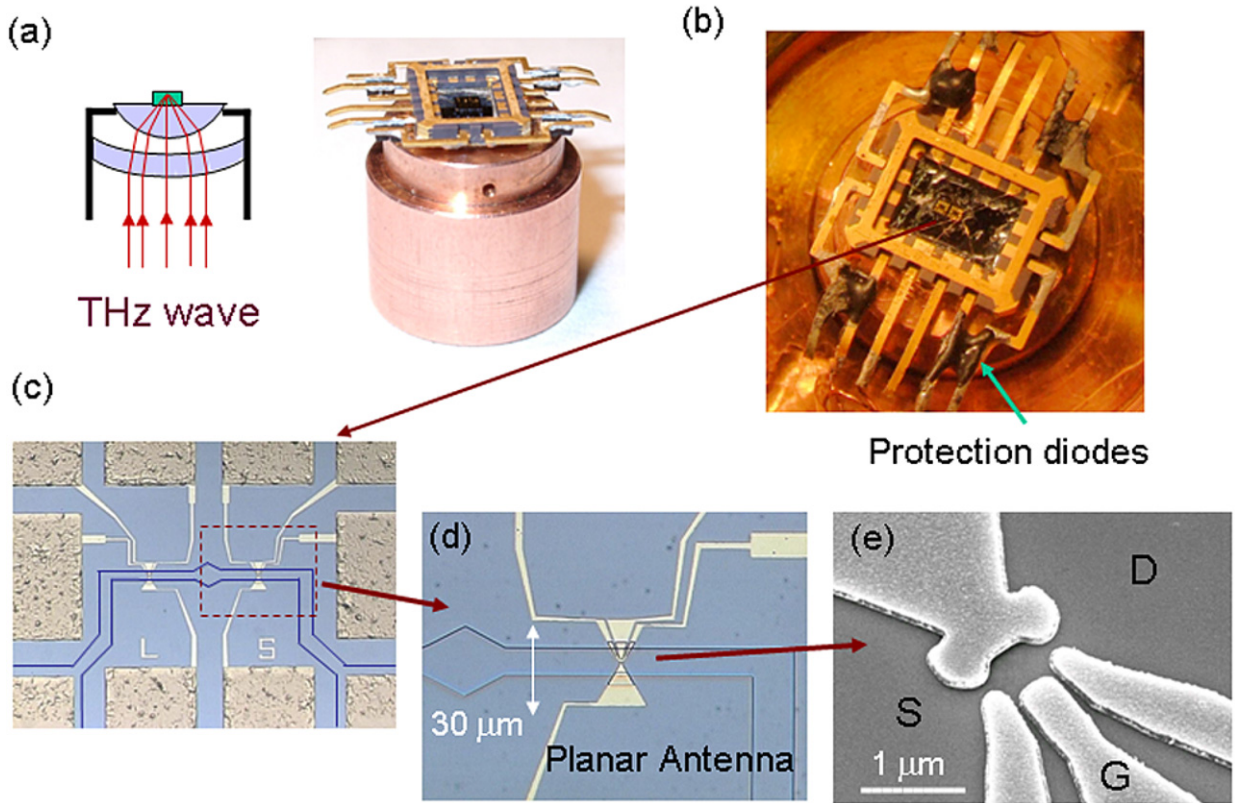
Fig. 3. Photographs of QD single THz photon detector embedded into an optical system.

(QW) structures (Charge Sensitive Infrared Phototoransistors, CSIP: $\lambda \sim 0.014$ mm or 21 THz) [14,15]. In the CSIP, the upper QW serves as a floating gate and a photo-induced charge in the upper QW is detected as a conductance change of the lower QW channels.

In this article, we focus on the Type-I QD detectors by which photon counting microscopy has been realized [16]. Fig. 3 shows photographs of the Type-I QD detector incorporated into an optical system. An aplanatic hyperhemispherical lens, made of silicon with a refractive index of $n_{Si} = 3.38$, is used for the substrate lens (Fig 3(a)). The QD detector is mounted on the focal spot with protection diodes (Fig. 3(b)). The incident photon flux enters from the backside of the QD detector, leading to the enhancement of the quantum efficiency as will be mentioned in the next section.

The QD detectors are fabricated from GaAs/AlGaAs single heterostructure crystals through standard electron beam lithography (Figs. 3(c)–3(e)). In the crystals, a two-dimensional electron gas (2DEG) layer is formed at the depth of about 100 nm from the surface. When the gates are negatively biased, the 2DEG layer is depleted from the region below the gates. A 2DEG island of 500 nm diameter with about 300 electrons is formed as shown in Fig. 4(a). Weakly coupled to two electron reservoirs (Source (S) and Drain (D)), the QD works as an SET. These gate electrodes also function as a planar dipole antenna (Fig. 4(b)). The trick of this detector is that we apply strong magnetic fields perpendicular to the plane of the QD. In the operation condition, the lowest $N = 0$ orbital Landau level (LL0) is completely filled, while the first excited $N = 1$ LL (LL1) is partially occupied with a small number of electrons. At the Fermi level, these LLs form two compressible metallic regions, an outer ring and an inner core as shown in Fig. 4(c). When the electrochemical potential of the outer ring lines up with that of the electron reservoirs, conductance resonance takes place because electrons tunnel between the reservoirs and the outer ring. The inner core does not directly contribute to the transport, but its charge strongly affects the transport through the capacitive coupling to the outer ring. When a THz photon is absorbed by the QD through cyclotron resonance, an electron is created in the LL1 and will rapidly fall to the inner core. In a similar way, a hole will climb up to the outer ring. This internal polarization causes the conductance–resonance peaks to shift towards the negative direction of gate voltage (compare Figs. 5(a) and 5(b)). This makes single THz photon detection feasible on a proper gate-voltage condition (Fig. 5(c)).

In the first demonstration of single-photon detection [9], a ^{3}He–^{4}He dilution refrigerator was used to achieve a long lifetime of the excited polarization at ultra low temperatures below 0.1 K. To construct a scanning THz microscope we use a more compact ^{3}He refrigerator, the base temperature of which is limited to 0.3 K. The lifetime of photo-excited polarization state of the QD is thereby reduced by a factor of about 10^{-2}, requiring a faster detection speed than that in the previous measurements applying a lock-in technique (1 msec). Because of this, the SET is here operated in a direct coupled mode as shown in the upper panel of Fig. 6. The current is detected as the voltage drop across a low-temperature resistance (40 kΩ)
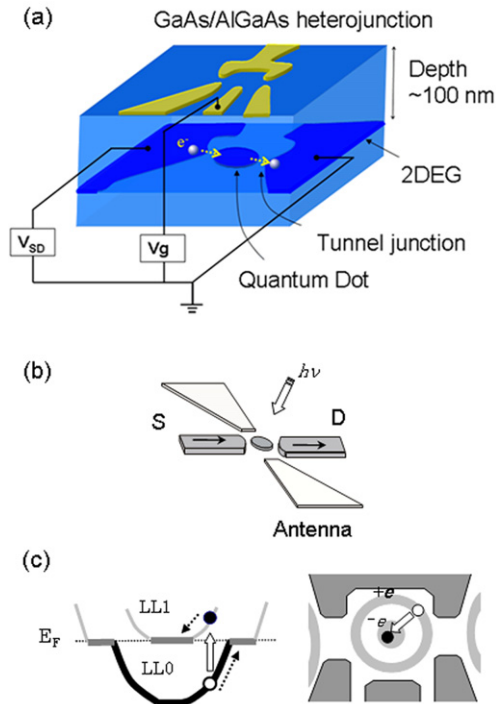
Fig. 4. Schematic representation of a semiconductor quantum dot serving as a single electron transistor (a). Metal gates work as a planar antenna (b). Energy profile of two-dimensional electrons in the quantum dot under a strong magnetic field (left). Landau levels form two conducting areas, an outer ring and an inner core of the quantum dot at the Fermi level (right) (c).
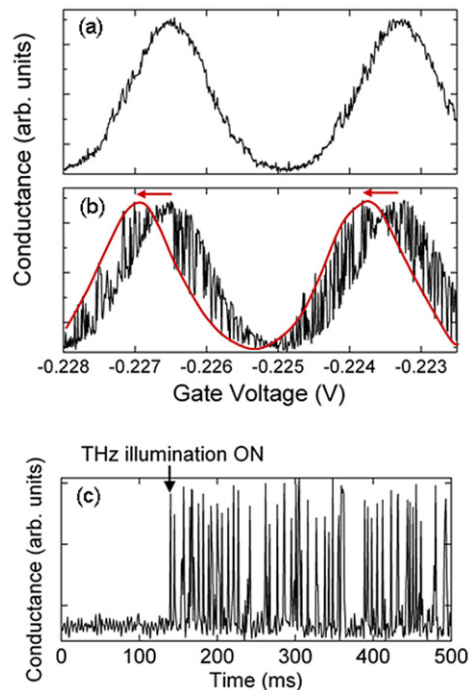
Fig. 5. SET conductance–resonance curve (a) without and (b) with THz illumination at $T = 0.3$ K and under $B = 5.45$ T. (c) Typical photon-counting signals measured at a fixed gate voltage (-0.224 V).

connected in series to the SET. By minimizing stray capacitance of wiring, the operation speed is improved to 20 µs (the bottom panel of Fig. 6) [16]. Figs. 5(a) and 5(b) show the conductance–resonance peaks without and with THz illumination at 0.3 K, respectively. Due to the improvement of SET operation speed, single photon absorption events distinctly give rise
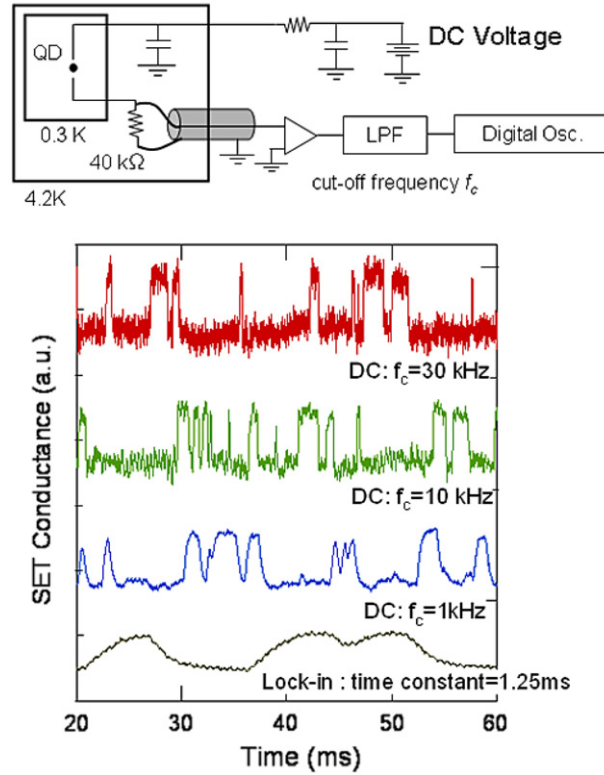
Fig. 6. (a) Schematic diagram of the direct-coupled readout circuit of the QD detector. (b) Real time trace of photon-counting signals (conductance switches) at $T = 0.3$ K. Four curves display results obtained via different amplifying schemes. A lock-in modulation technique yields a response time constant of $\tau_c = 1.25$ ms (bottom). Faster response with $\tau_c = 600$ μs, 60 μs and 20 μs (middle and top) is obtained in a constant voltage mode, where f_c denotes the cut off frequency of low-pass filters used.

to telegraph-like conductance switches at 0.3 K as shown in Fig. 5(c). The dark switching rate at 0.3 K is 0.1 count per second (cps) in the best condition, corresponding to noise equivalent power, 10^{-21}–10^{-20} W/Hz$^{1/2}$. The faster detection speed leads also to the improvement of the linear dynamic range beyond 30 dB, but this can be expanded furthermore. The intrinsic limit on the speed of the SET is greater than 10 GHz. In practice, using the high-frequency operation scheme of SET [17] will improve the time resolution up to a 10-MHz range.

The upper bound of the operation temperature is limited by the charging energy of the QD (about 0.4 meV for the size of our QD's). The upper bound is hence about 0.4 K. Replacing the charge sensitive transistor by a quantum point contact (QPC) or a narrow channel FET may expand the upper bound to 1.5 K or 4.2 K [18,15]. In this regard, however, the incident photon rate from 6 K back ground radiation will be far beyond the dark switching rate W_{dark} of the QD detectors in the long wavelength range exceeding 0.1 mm. Therefore, despite the detection mechanism, cooling the detector (and its surrounding environment) down to 4.2 K will be necessary for making the photon counter fulfill its performance.

The effective sensitivity of photon counters is determined by the quantum efficiency η along with the dark switching rate W_{dark}, given by $NEP = h\nu\sqrt{2W_{dark}}/\eta$ [W/Hz$^{1/2}$]. In the QD detectors, the incident THz waves are coupled to a small QD through a planar dipolar bow-tie antenna, formed by metal gates (Fig. 4(b)). The quantum efficiency is hence determined by the coupling between the QD and the planar antenna. When radiation falls from vacuum onto a planar antenna fabricated on a dielectric medium of the dielectric constant of $\epsilon = 12$, most of the radiation power is reflected: the power ratio of the reflected part to the penetrating part is $\epsilon^{3/2}$. Additionally considering the impedance matching of antenna to the QD, the quantum efficiency is roughly estimated to be $\eta = 0.1$–1% [19]. With the dark switching rate $W_{dark} = 0.001$ s^{-1} at 70 mK, the NEP reaches an order of 10^{-21} [W/Hz$^{1/2}$]. Since the effective photoactive area S of the QD detectors is determined by the wavelength λ_ϵ in the dielectric medium, the specific detectivity D^* is estimated to be 10^{18} [cm Hz$^{1/2}$/W]. As just described, even taking account of the poor quantum efficiency, the sensitivity of QD detectors is several orders of magnitude higher than the best values of conventional detectors used in Astronomy.

3. Photon counting THz imaging

3.1. Scanning confocal THz microscope

We have developed a scanning confocal THz microscope for fundamental scientific research of low-dimensional semiconductors (Fig. 7) [16]. The detector, embedded into an optical probe (Fig. 3(a)), is cooled down to ^{3}He temperatures
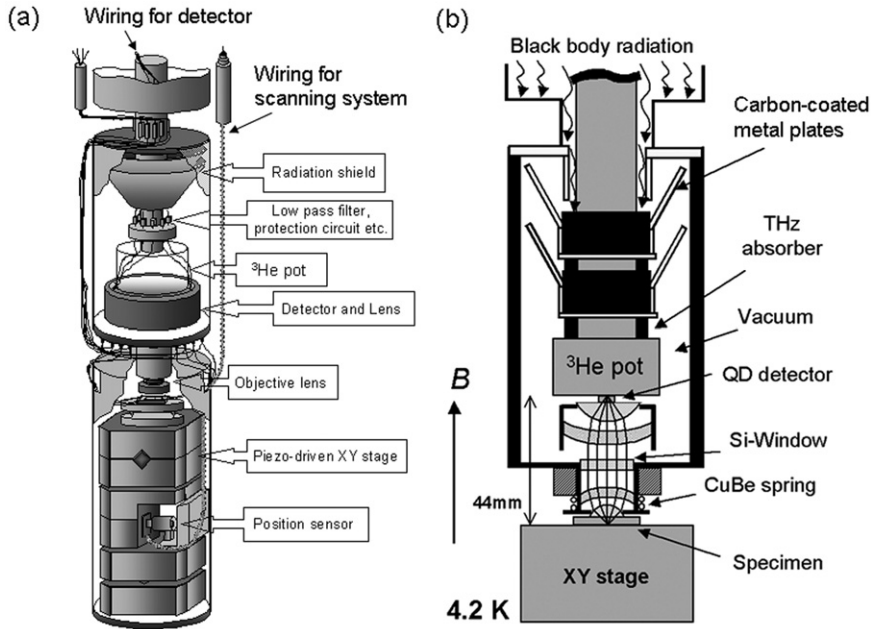
**Fig. 7.** Schematics of the scanning-type THz microscope with a single photon counter.

($T \simeq 0.3$ K) while thermally insulated by vacuum from the object (a quantum Hall effect (QHE) device) placed at a higher temperature. In the present prototype, the temperature of the object is 4.2 K, but higher temperatures may be possible owing to the vacuum insulation. Both the objective lens system and the detector lens system are a coupled silicon hyperhemisphere lenses designed to be aplanatic. THz radiation falls from the dielectric medium onto the planar antenna of detector (Figs. 3(a) and 7(b)), leading to significant improvement of the quantum efficiency up to several tens of percent. Therefore, the sensitivity of $NEP = 10^{-21}$–10^{-20} [W/Hz$^{1/2}$] ($D^* \sim 10^{18}$ [cm/Hz$^{1/2}$/W]) is kept at the base temperature of ^{3}He refrigerator, even though the dark switching rate rises to $W_{dark} = 0.1$ s^{-1} at 0.3 K.

In the objective lens system, a solid immersion lens (SIL) is moderately pushed onto the backside of the sample by a CuBe spring. THz waves emitted from the sample at the focal point of the SIL are transmitted through a silicon window and refocused on the detector. By moving the sample with a piezo-driven XY stage, the focal point scans the whole area of the device. Two-dimensional pictures of THz radiation on an atto-watt level ($\sim 10^3$ photons per second), are thus obtained. Owing to the aplanatic lens system, a resolution of 0.05 mm is achieved for a free-space wavelength of $\lambda_0 = 0.13$ mm. Here, the effective sensitivity of this microscope system, including the loss of optical lenses, is roughly estimated to be 10^{19} [W/Hz$^{1/2}$]. Therefore, this microscope makes it possible to detect extremely weak THz radiation (corresponding to one hundred photons per second) emitted from an area of $\sim (\lambda/3)^2$.

In actual measurements, we need to pay much attention to suppressing both electrical and optical background noise. To avoid electrical coupling between the QD detector and high voltage lines, all twisted pairs and coax cables for scanning the piezo-driven XY stage in the microscope are wired outside the ^{3}He insert with multiple shields as shown in Fig. 7(a). On the other hand, shielding of the high-temperature black body radiation is important for the vacuum space, to which the detector is exposed. Multiple carbon-coated metal plates are thereby introduced. To cover a wider dynamic range of radiation intensity, we also use a simpler microscope with QHE detectors [20], which are narrow band ($\Delta\lambda/\lambda \simeq 0.025$) and magnetically tunable ($\lambda = 110$–140 μm) integration type sensors, applicable in the dynamic range of 10^{-15}–10^{-12} watts. Applied to the study of quantum Hall electron systems, these THz microscope systems reveal a variety of new features in the kinetics of nonequilibrium electron generation. Characteristic spatial patterns of nonequilibrium electron distribution are visualized as 2D images of THz radiation, along with their evolution with varying the gate voltage or the current. Spectroscopic studies further clarify the energy distribution of nonequilibrium electrons with location-specific, which extracts electron population dwelling in the higher discrete energy levels.

3.2. THz imaging of quantum Hall effect devices

The 2DEG in strong magnetic fields (B) offers us a unique object for passive THz microscopy. The orbital motion of electrons in strong B is a cyclic cyclotron motion, the kinetic energy of which is split into discrete LLs separated by cyclotron energy $\hbar\omega_c = eB/m^*$ ($\hbar = h/(2\pi)$ with Planck's constant h and m^* the cyclotron effective mass of the 2DEG). An integer number N ($= 0, 1, 2, \ldots$) of LLs is filled with 2DEG if the filling factors of LLs, $\nu = hn_{2D}/(eB)$, takes integer value N, where n_{2D} is the density of electrons. In this integer QHE state, the longitudinal resistance (proportional to the voltage drop along the current direction) vanishes and the Hall resistance is quantized. Accordingly, THz emission should be absolutely
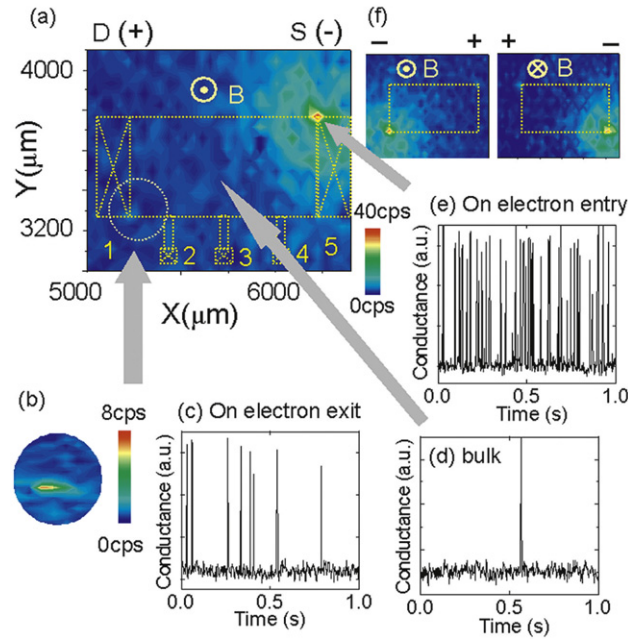
Fig. 8. Photon-counting THz imaging of cyclotron emission from a QH device. (a) THz-photon counts per second (cps), detected in the $\nu = 2.00$ QH state ($B = 5.62$ T) at 1.2 μA ($eV_{15} = 15.5$ meV), are colour mapped (red, 40 cps; blue, 0 cps). The broken line illustrates a 1 mm-long and 0.5 mm-wide Hall-bar studied, fabricated on a GaAs/AlGaAs heterojunction ($n_{2D} = 2.7 \times 10^{15}$ m^{-2}, $\mu = 27$ m^2/Vs). The THz waves are of $\hbar\omega_c = 8.94$ meV ($\omega_c = 2\pi \times 2.16$ THz) or the wavelength of 139 μm. (b) The emission on the drain corner is visible when the sensitivity is enhanced in presentation. The XY scale is expanded by a factor of 1.5. (c), (d) and (e) SET conductance switches due to photon absorption for different positions, drain corner (c), bulk region (d), and source corner (e). (f) The photon count rate versus the source-drain bias voltage (bottom axis) or the current (top axis). The red and the green data points represent the data on the source and the drain corners, respectively.

absent in the QHE states, because the electron system is deemed to be in the dissipation-less state. However, if, for some mechanism, nonequilibrium electrons (holes) are generated in LLs above (below) the Fermi level, they release a part of their excess energy via radiative recombination process. This manifests itself as the emission of THz photons with the cyclotron energy. Therefore, the passive THz microscopy provides us with an extremely sensitive experimental tool to explore the mechanism of excitation and to probe local density profile of the excited nonequilibrium electrons.

Fig. 8 shows photon-counting images of the cyclotron radiation, in which the 2DEG condenses in the QHE states of $\nu = 2$ at $B = 5.62$ T ($\hbar\omega_c = 8.94$ meV) and 1.2 μA (the source-drain bias $V_{15} = 15.5$ mV) [16]. The radiation intensity is colour coded by counting the events of SET-current switching (Figs. 8(c)–8(e)). Although emission is not discerned in the interior region of the Hall-bar, two bright spots are recognized on the diagonally opposite two corners of the current contacts. A brighter spot is on the electron entry corner near the source contact and a less-bright one is on the exit corner of the drain. In earlier measurements, the emission could be seen only when an array of more than 10 000 Hall bars was studied (otherwise, much larger currents (> 50 μA) are needed) [21]. Since the sensitivity is practically unlimited here, we are now able to see the emission from a single Hall bar, and track the emission down to sub-μA level. As shown in Fig. 9, a distinct threshold is found at $V_{15} = \hbar\omega_c/(2e) = 4.5$ mV (0.35 μA) for the emission at source corner, and at $V_{15} \simeq \hbar\omega_c/e \simeq 9.0$ mV (0.7 μA) for the emission at drain corner. These new findings can be interpreted as follows. Nonequilibrium electrons can be generated via electron-tunnelling through electrostatic potential barrier (or fall) formed at the entry (or the exit) corner. On the entry corner, the electrochemical potential of the source lines up with the empty $N = 1$ LL when eV_{15} reaches $\hbar\omega_c/2$, and the tunnelling through the barrier is hence permitted. On the exit corner, however, we expect that the tunnelling process originates from the inter-LL-transition within the potential fall, and therefore a bias beyond $\hbar\omega_c$ is required.

Another phenomenon of nonequilibrium electron generation disclosed by the photon-counting method is the effect of unequally populated edge channels [22–24]. A metal cross gate is deposited in a Hall-bar shown in Fig. 10(a). With $B = 4.98$ T ($\hbar\omega_c = 7.92$ meV), the filling factor is $\nu_B = 4.0$ in the bulk region while a negative gate bias voltage assigns $\nu_G = 2.0$ to the region beneath the gate. In this condition, the edge channel of the upper LL ($N = 1$) is perfectly reflected at the potential barrier formed by the gate, while the other edge channel of the lowest LL ($N = 0$) is transmitted through the barrier (Fig. 10(b)). Different edge channels are thus unequally populated, and a variety of effects have been extensively studied in resistance measurements. However, cyclotron emission has never been seen because photon-level sensitivity was necessary. As shown in Fig. 10(c), emission is found to occur at the diagonally opposite points of confluence for the unequally populated edge channels [25]. It is found that the spot on the lower-potential boundary for electrons (with positive Hall voltage) is brighter than the other: The imaging pictures taken in the opposite magnetic-field polarities (Fig. 10(c)) show that this is an intrinsic property. As shown in Fig. 10(d), the less emissive spot is easier to interpret: The emission is characterized by
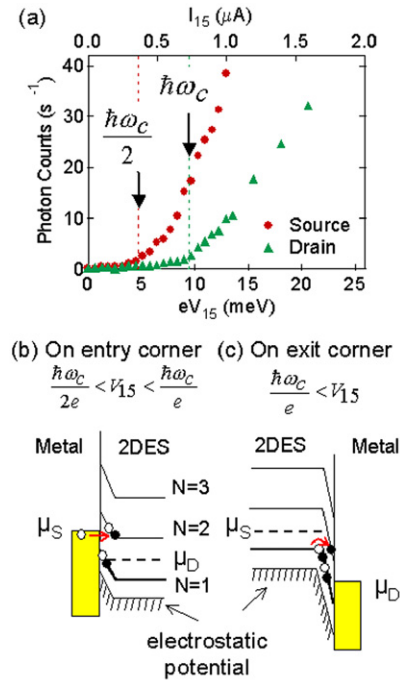
Fig. 9. Characteristics in the threshold regime of photon emission. (a) Photon-count rate versus the source-drain bias voltage (bottom axis): The values of current are marked on the top axis. The circles and the triangles represent the data on the source and the drain corners, respectively. (b) and (c) Schematic representations of the energy profile on the electron entry corner at $\hbar\omega_c/(2e) < V_{15} < \hbar\omega_c/e$ and on the exit corner at $\hbar\omega_c/e < V_{15}$.
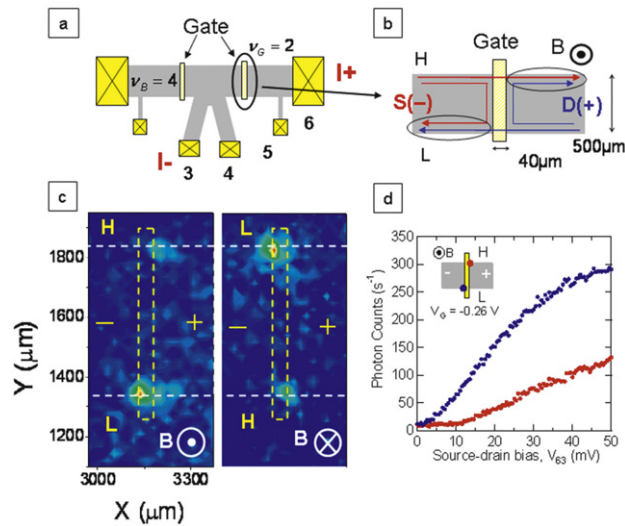
Fig. 10. Cyclotron emission from the inter-edge nonequilibrium produced by a potential barrier. (a) Schematic of the sample with two metal gates of 40 μm-width across the 2DEG channel, fabricated on a GaAs/AlGaAs heterojunction ($n_{2D} = 3.8 \times 10^{15}$ m^{-2}, $\mu = 150$ m^2/Vs). The filling factors are $\nu_B = 4$ ($B = 4.98$ T, $\hbar\omega_c = 7.92$ meV) in the bulk region while $\nu_G = 2$ underneath the gates (negative bias of -0.26 V). The n_{2D} of the sample is adjusted to the available range of the QD detector by a light-emitting diode illumination (GaAs-LED). The currents are applied between 6 and 3, and only a gate on the right-hand side is used. (b) Representation of edge-channels. The edge channel of the $N = 1$ LL ($N = 0$ LL) is reflected (transmitted), where the spin-resolved edge channels are ignored. The red (blue) lines correspond to edge channels with higher (lower) electrochemical potential imposed by the source (drain)-potential. The elliptic circles mark the sample boundaries along which different edge channels are unequally populated. (c) Photon-counting THz images of cyclotron emission in the gate region at $V_{63} = 12.9$ mV ($I_{63} = 1.0$ μA). When the polarization of magnetic field is reversed, the higher (lower) potential side of sample boundaries, designated as H (L), is interchanged. (d) The photon count rate versus the source-drain bias. Blue (red) lines show the data taken at the corner spots indicated in the inset with the same colour. The background counts (about 11 cps) are attributed to the dark switching of SET currents.
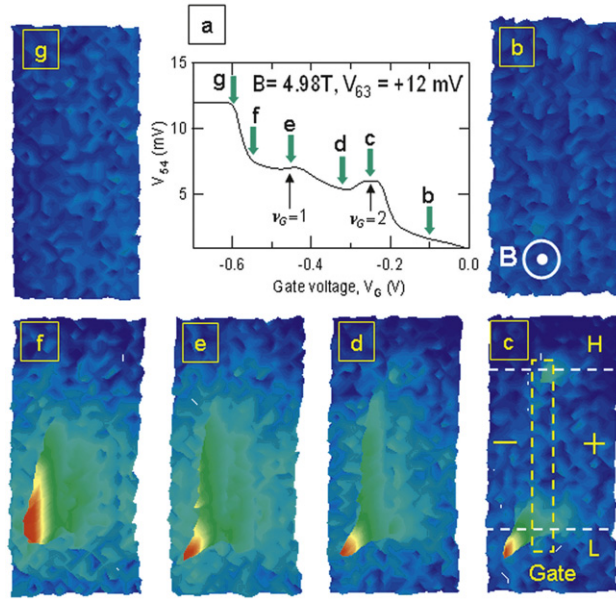
Fig. 11. Barrier-height dependence of cyclotron emission profile. (a) Gate-bias dependence of the four-terminal voltage, V_{54}, at a source-drain bias of $V_{63} = 12$ mV and $\nu_B = 4$ ($B = 4.98$ T). (b)–(g) 3-dimensional (3D) views of THz imaging at 25.8 mV ($I_{63} = 2.0$ μA), taken at different gate bias voltages shown with green arrows in (a).
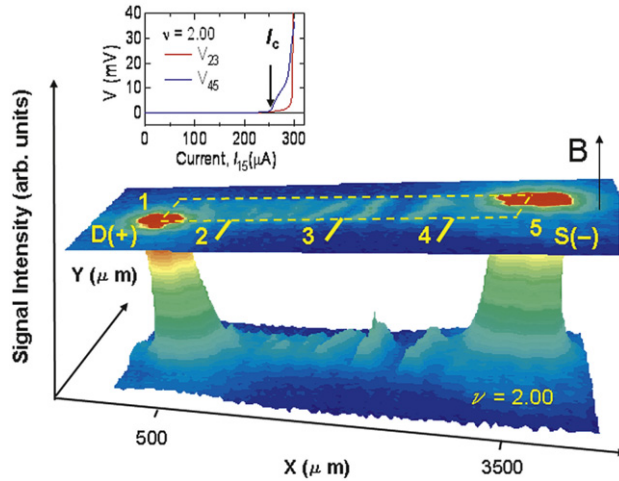
Fig. 12. THz imaging in QHE breakdown regime. (a) 3D picture of the THz image in the breakdown regime of $I_{15} = 300$ μA and $\nu = 2.00$ ($B = 6.14$ T), where a THz microscope with a QHE detector is used. The sample studied is a 3 mm × 0.5 mm Hall-bar (GaAs/AlGaAs heterojunction; $n_{2D} = 3.0 \times 10^{15}$ m^{-2}, $\mu = 30$ m^2/Vs). The cyclotron energy is 9.77 meV (2.36 THz or a wavelength of 127 μm). The narrow-band and tunable QHE detector (0.4 × 0.4 mm) fabricated in a GaAs/AlGaAs heterojunction ($n_{2D} = 2.7 \times 10^{15}$ m^{-2}, $\mu = 100$ m^2/Vs) is used. The inset shows longitudinal voltages, V_{23} and V_{45}, as a function of current, I_{15} in the Hall-bar at $\nu = 2.00$. The arrow marks the critical current, $I_c = 250$ μA, at which the QHE breaks down.

the presence of a threshold voltage, corresponding to a value of $\Delta\mu_{noneq}$ slightly higher than $\hbar\omega_c$ (8 meV or $I_{63} \sim 1.2$ μA), where $\Delta\mu_{noneq}$ is the electrochemical potential difference between the two edge channels.

The threshold value of $\Delta\mu_{noneq}$ for the emissive spot, if any, is substantially smaller than $\hbar\omega_c$, which requires our deeper understanding. Interestingly, as the potential barrier is pushed up higher (Fig. 11), the emissive region progressively evolves upstream along the $N = 1$ edge channel (originating from the source contact). Earlier studies by applying fountain-pressure effect of superfluid liquid helium show that the higher-potential spot (the less-emissive spot in Fig. 10(c)) is more energy-dissipative and the lattice is heated more significantly, which is supported by theoretical considerations [26]. The experimental findings here thus require deeper theoretical understanding of the generation mechanism of nonequilibrium electrons, which takes into account self-consistently the formation of potential barrier, redistribution of edge/bulk states [27] and the charge neutrality condition [26].
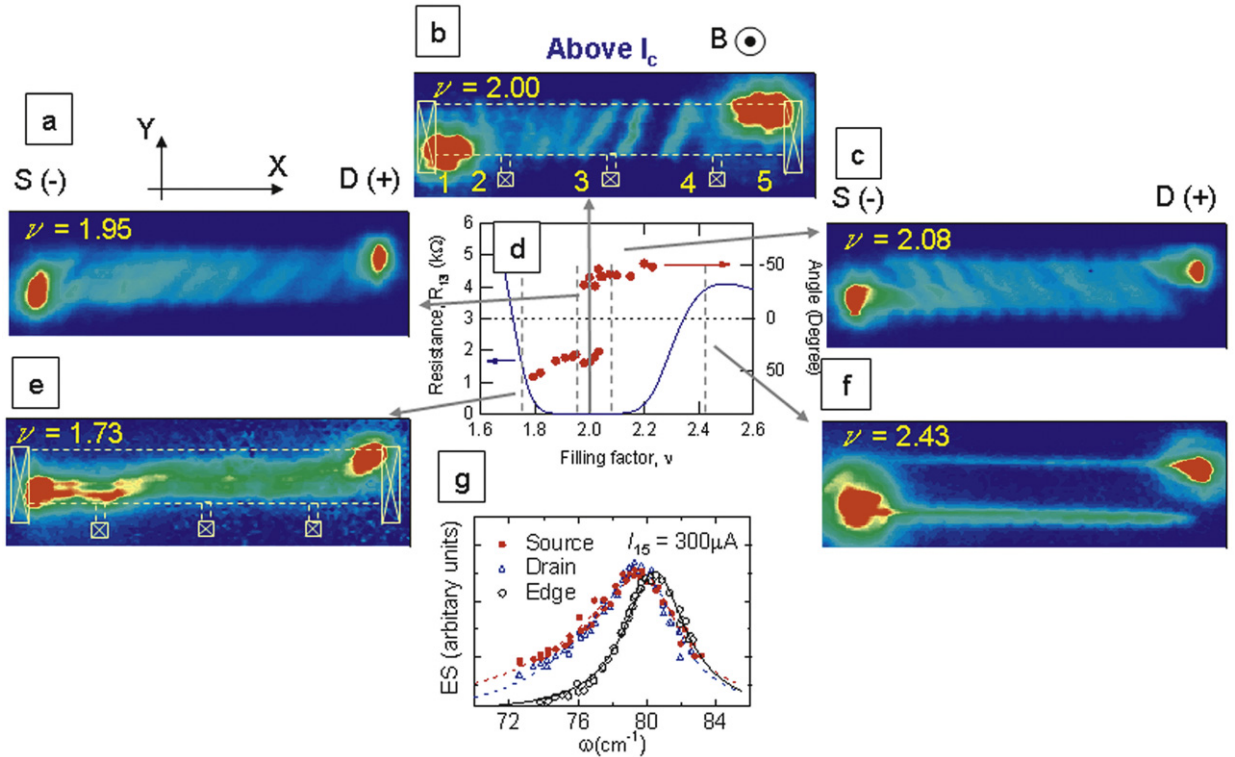
Fig. 13. Different spatial patterns of nonequilibrium electron distribution in a large-current regime. (a)–(c) THz images in the QHE breakdown regime: $\nu = 1.95$ ($B = 6.29$ T) and $I_{15} = 250$ μA (a), $\nu = 2.00$ ($B = 6.14$ T) and $I_{15} = 300$ μA (b), and $\nu = 2.08$ ($B = 5.90$ T) and $I_{15} = 250$ μA (c). In (b), broken lines mark the outline of the Hall-bar. (d) The tilt angle of the stripes (red dots) against ν. The angle is defined as positive if the stripes are tilted clockwise from the y-axis. The longitudinal resistance, R_{13}, is shown together with a blue line. (e) and (f) THz images in transition regions: $\nu = 1.73$ ($B = 6.15$ T) and 250 μA with guide lines of the Hall-bar; (e); $\nu = 2.43$ ($B = 6.14$ T) and 200 μA (f). In order to adjust the magnetic field to a suitable range for the QHE detector, ns of the sample is tuned via illumination by GaAs-LED and negative biasing of backgate. (g) The spectra of cyclotron emission at different positions in the Hall-bar (red circles; source corner, blue triangles: drain corner, and black circles; along the edge).

Yet another important driving force for generating nonequilibrium electrons is the bias current itself. The dissipation-less character of the QHE conductor abruptly collapses when the current exceeds a critical value I_c: The longitudinal resistance suddenly increases accordingly (in the insert of Fig. 12) [28]. The origin of this current-induced breakdown is a thermal instability of the electron system, and manifests itself as avalanche-type electron–hole pair multiplication via inter-LL impact ionization [29–31]. Slow evolution of excited carrier multiplication has been disclosed in transport measurements [31]. However, the profile of spatial distribution of excited carriers has not been well clarified because transport measurements do not probe excited electrons in the interior region of Hall bars. Since the breakdown of the QHE is a consequence of electron (hole) generation in LLs above (below) the Fermi level, the cyclotron radiation gives a local probe to the phenomenon. In this measurement, we use another scanning THz microscope with a QHE detector [20], which is more suitable for subpico-watt level radiation. Fig. 12 is a 3D THz image of a Hall bar in a breakdown regime of $\nu = 2.00$ with a current of 300 μA (above the critical value). In addition to the two bright regions near the corners of current contacts, a distinct stripe pattern is unearthed in the interior region of the Hall-bar. Furthermore, the stripes are tilted from the vertical direction (Figs. 13(a)–13(c)). The tilt angle reverses its sign when the filling factor crosses the point of exact two (Fig. 13(d)).

These results, without interpretation, definitely indicate self-organized pattern formation of nonequilibrium electrons in the breakdown regime. Additional experiments confirm that each stripe is accompanied with a finite longitudinal resistance. The electron system with a current not too far from the critical value is expected to be in bistable states [29,30], in which a lower electron temperature state corresponds to the dissipation-less QHE state while a higher electron temperature state to the dissipative breakdown state. In such a bistable state, it may be possible that spatiotemporal structure is self-organized [32]. The THz microscopy here clarifies that a spatially varying, but stationary, striped pattern is formed. The relatively regular structure found here may be suggested to be the origin of the earlier reported "quantized longitudinal resistance" found in resistance measurements [33]. We suppose that the tilt angle of the stripe is determined by the direction of heat flow. The heat is carried predominantly by excited holes and electrons, respectively, for $\nu < 2$ (Fig. 13(a)) and $2 < \nu$ (Fig. 13(c)). While the direction of electrical current is unaltered whether the carries are electrons or holes, the heat flow reverses its direction when the carrier changes from holes to electrons at $\nu = 2$.

In B-regions outside the QHE states (far away from $\nu = 2$), the characteristic profile of THz emission is largely different (Figs. 13(e) and 13(f)). When ν is substantially larger than 2, partially occupied $N = 1$ LL forms edge channels along the

opposite boundaries of the Hall bar. It follows that the sample boundaries become bright due to edge-bulk nonequilibrium (Fig. 13(e)). When ν is substantially smaller than 2, there are no edge channels in the Hall bar, so that the THz emission is present only in the interior region (Fig. 13(f)).

An important ability of our microscopes is spectroscopy. In all the THz-emissions discussed so far, the relevant transition is between the lowest two LLs, viz., $N = 1 \to 0$. The emission spectrum is therefore analogous to the absorption line spectrum. Fig. 13(g) illustrates emission spectra in the electron entry and exit corners at a high current, which are studied for the energy spectroscopy of electrons. The spectra are significantly broadened towards lower frequencies while a symmetric lineshape is obtained along the edge. This is because energetic electrons are excited in higher LLs, and transitions of $N = 4 \to 3$, $3 \to 2$ and $2 \to 1$ are relevant. The higher transitions yield lower frequency components through the conduction-band nonparabolicity of GaAs [34].

4. Conclusion

Passive THz microscopy thus sheds new lights on QHE devices. Its application, however, may not be restricted to low-temperature semiconductor devices, but should go far beyond. Operation without magnetic fields is possible by using another type of QD detector. Studying objects at elevated temperatures, even up to room temperature, may not be a dream far out of reach, if the spatial resolution is significantly improved. A nano-meter resolution may be achieved by applying near-field techniques exploiting micro metal-tip antennas, as demonstrated in mid- and far-infrared regions [35–37]. The microscope system would be further improved by minimizing the stray radiation originating from the regions other than the focal point reaching the detector. We note that Plank's law of black body radiation applies to the materials of maximal emissivity. Constructing all the parts located in the vicinity of the object in study with low emissivity (transparent) materials may greatly help to reduce the background level of black body radiation. Given a microscope of higher resolution with low background level of black body radiation, a variety of challenging applications will be opened up. Individual molecular dynamics in chemical reactions or nondisturbed biological activities may be targeted. Living organisms are active at room temperature, and so they may be using thermal energy (or thermal fluctuation) in an efficient manner for the sake of their own activities via specific modes of excitation. Since most of biological molecules are of electrical polarization, the intrinsic information on their spontaneous motions would be emitted towards the environment in the form of THz radiation. Even at a least level of improvement, microthermography revealing local temperature distribution may provide us with new findings of cell activities. For instance, if a single ATP molecule is hydrolysed in an environment surrounded by a numerous number of water molecules, possible rise in the local temperature should be substantial.

Acknowledgements

References

[1] P.R. Smith, D.H. Auston, M.C. Nuss, Subpicosecond photoconducting dipole antennas, IEEE J. Quantum Electron. 24 (1988) 255–260.

[2] B.B. Hu, M.C. Nuss, Imaging with terahertz waves, Opt. Lett. 20 (1995) 1716–1718.

[3] R. Köhler, A. Tredicucci, F. Beltram, H.E. Beere, E.H. Linfield, A.G. Davies, D.A. Ritchie, R.C. Iotti, F. Rossi, Terahertz semiconductor-heterostructure laser, Nature 417 (2002) 156–159.

[4] D.M. Mittleman, R.H. Jacobsen, M.C. Nuss, T-ray imaging, IEEE J. Select. Topics Quantum Electron 2 (1996) 679–692.

[5] S. Wang, B. Ferguson, D. Abbott, X.-C. Zhang, T-ray imaging and tomography, J. Biol. Phys. 29 (2003) 247–256.

[6] K. Kawase, Y. Ogawa, Y. Watanabe, H. Inoue, Non-destructive terahertz imaging of illicit drugs using spectral fingerprints, Optics Express 11 (2003) 2549–2554.

[7] A. Lipatov, O. Okunev, K. Smirnov, G. Chulkova, A. Korneev, P. Kouminov, G. Gol'tsman, J. Zhang, W. Slysz, A. Verevkin, R. Sobolewski, An ultrafast NbN hot-electron single-photon detector for electronic applications, Supercond. Sci. Technol. 15 (2002) 1689–1692.

[8] J. Wei, D. Olaya, B.S. Karasik, S.V. Pereverzev, A.V. Sergeev, M.E. Gershenson, Ultrasensitive hot-electron nanobolometers for terahertz astrophysics, Nature Nanotechnology 3 (2008) 496–500.

[9] S. Komiyama, O. Astafiev, V. Antonov, T. Kutsuwa, H. Hirai, A single-photon detector in the far-infrared range, Nature 403 (2000) 405–407.

[10] O. Astafiev, S. Komiyama, T. Kutsuwa, V. Antonov, Single-photon detector in the microwave range, Appl. Phys. Lett. 80 (2002) 4250–4252.

[11] V. Antonov, O. Astafiev, T. Kutsuwa, H. Hirai, S. Komiyama, Single FIR-photon detection using a quantum dot, Physica E 6 (2000) 367–370.

[12] H. Hashiba, V. Antonov, L. Kulik, A. Tzalenchuk, P. Kleinshmid, S. Giblin, S. Komiyama, Isolated quantum dot in application to terahertz photon counting, Phys. Rev. B 73 (2006) 081310(R).

[13] J.C. Chen, Z. An, T. Ueda, S. Komiyama, K. Hirakawa, V. Antonov, Metastable excited states of a closed quantum dot probed by an aluminum single-electron transistor, Phys. Rev. B 74 (2006) 045321.

[14] Z. An, T. Ueda, S. Komiyama, K. Hirakawa, Metastable excited states of a closed quantum dot with high sensitivity to infrared photons, Phys. Rev. B 75 (2007) 085417.

[15] T. Ueda, Z. An, K. Hirakawa, S. Komiyama, Charge sensitive infrared phototransistors: Characterization by an all-cryogenic spectrometer, J. Appl. Phys. 103 (2008) 093109.

[16] K. Ikushima, Y. Yoshimura, T. Hasegawa, S. Komiyama, T. Ueda, K. Hirakawa, Photon-counting microscopy of terahertz radiation, Appl. Phys. Lett. 88 (2006) 152110.

[17] R.J. Schoelkopf, P. Wahlgreen, A.A. Kozhevnikov, P. Delsing, D.E. Prober, The radio-frequency single-electron transistor (RF-SET): a fast and ultrasensitive electrometer, Science 280 (1998) 1238–1241.

[18] S. Pelling, R. Davis, L. Kulik, A. Tzalenchuk, S. Kubatkin, T. Ueda, S. Komiyama, V.N. Antonov, Point contact readout for a quantum dot terahertz sensor, Appl. Phys. Lett. 93 (2008) 073501.

[19] O. Astafiev, S. Komiyama, Single-photon detection with quantum dots in the far-infrared/submillimeter-wave range, in: J.P. Bird (Ed.), Electron Transport in Quantum Dots, Kluwer Academic Publishers, 2003, pp. 363–396.

[20] K. Ikushima, H. Sakuma, S. Komiyama, A highly sensitive scanning far-infrared microscope with quantum Hall detectors, Rev. Sci. Instrum. 74 (2003) 4209–4211.

[21] Y. Kawano, Y. Hisanaga, S. Komiyama, Cyclotron emission from quantized Hall devices: Injection of nonequilibrium electrons from contacts, Phys. Rev. B 59 (1999) 12537–12546.

[22] B.J. van Wees, et al., Anomalous integer quantum Hall effect in the ballistic regime with quantum point contacts, Phys. Rev. Lett. 62 (1989) 1181–1184.

[23] S. Komiyama, H. Hirai, S. Sasa, S. Hiyamizu, Violation of the integral quantum Hall effect: Influence of backscattering and the role of voltage contacts, Phys. Rev. B 40 (1989) 12566–12569.

[24] R. Haug, A.H. MacDonald, P. Streda, K. von Klitzing, Quantized multichannel magnetotransport through a barrier in two dimensions, Phys. Rev. Lett. 61 (1989) 2797–2800.

[25] K. Ikushima, S. Komiyama, T. Ueda, K. Hirakawa, THz-photon generation due to electrons injected via quantum-Hall edge channels, Physica E 40 (2008) 1026–1029.

[26] S. Komiyama, et al., Inter-edge-state scattering and nonlinear effects in a two-dimensional electron gas at high magnetic fields, Phys. Rev. B 45 (1992) 11085–11107.

[27] K. Ikushima, H. Sakuma, S. Komiyama, K. Hirakawa, Imaging of cyclotron emission from edge channels in quantum Hall conductors, Phys. Rev. Lett. 93 (2004) 146804.

[28] M.E. Cage, R.F. Dziuba, B.F. Field, E.R. Williams, S.M. Girvin, A.C. Gossard, D.C. Tsui, R.J. Wagner, Dissipation and dynamic nonlinear behavior in the quantum Hall regime, Phys. Rev. Lett. 51 (1983) 1374–1377.

[29] A. Gurevich VI, R.G. Mints, Nonlinear waves under conditions of the quantum Hall effect, JETP Lett. 39 (1984) 381–384.

[30] S. Komiyama, T. Takamasu, S. Hiyamizu, S. Sasa, Breakdown of the quantum Hall effect due to electron heating, Solid State Commun. 54 (1985) 479–484.

[31] S. Komiyama, Y. Kawaguchi, T. Osada, Y. Shiraki, Evidence of nonlocal breakdown of the integer quantum Hall effect, Phys. Rev. Lett. 77 (1996) 558–561.

[32] A. Gurevich VI, R.G. Mints, Self-heating in normal metals and superconductors, Rev. Mod. Phys. 59 (1987) 941–999.

[33] M.E. Cage, G.M. Reedtz, D.Y. Yu, C.T. van Degrift, Quantized dissipative states at breakdown of the quantum Hall effect, Semicond. Sci. Technol. 5 (1990) 351–354.

[34] W. Zawadzki, C. Chaubet, D. Dur, W. Knap, A. Raymond, Cyclotron emission study of electron masses in GaAs-GaAlAs heterostructures, Semicond. Sci. Technol. 9 (1994) 320–328.

[35] B. Knoll, K. Keilmann, Near-field probing of vibration absorption for chemical microscopy, Nature 399 (1999) 134–137.

[36] Chen Hou-Tong, R. Kersting, G.C. Cho, Terahertz imaging with nanometer resolution, Appl. Phys. Lett. 83 (2003) 3009–3011.

[37] Y. De Wilde, F. Formanek, R. Carminati, B. Gralak, P. Lemoine, K. Joulain, J. Mulet, Y. Chen, J. Greffet, Thermal radiation tunneling microscopy, Nature 444 (2006) 740.